RSC Advances

PAPER

View Article Online
View Journal | View Issue

Cite this: *RSC Adv.*, 2022, **12**, 30829

Evaluation of cytotoxic properties of two fluorescent *fac*-Re(CO)$_3$ complexes bearing an *N*,*N*-bidentate benzimidazole coligand†

Ahmed M. Mansour, *[a] Nourhan M. Ibrahim,[a] Ahmad M. Farag [a] and Mahmoud T. Abo-Elfadl [bc]

Received 22nd September 2022
Accepted 19th October 2022

DOI: 10.1039/d2ra05992d

rsc.li/rsc-advances

The reaction between 1*H*-benzimidazol-2-ylmethyl-(*N*-aryl)amine derivatives (L^R) and [ReBr(CO)$_5$] afforded octahedral Re(I) complexes of the general formula of [ReBr(CO)$_3L^R$] (R = 4-Cl and 4-COOCH$_3$). The Re(I) complexes were screened for their potential cytotoxicity against three malignant cell lines and one normal cell line of different origins. The solvatochromic characteristics of the complexes were examined by UV/vis. spectroscopy with the aid of time-dependent density functional theory calculations. Strong autofluorescence emission can be seen in the two Re(I) complexes between 460 and 488 nm. They appeared to accumulate inside intercellular connections and surrounding cellular membranes. The substances gathered also, along the cell membrane, waiting for their entry. The mode of cell death staining and the DNA fragmentation analysis revealed that the 4-Cl complex showed increased apoptotic changes in the MCF-7, and the Caco-2 cell line, while the HepG2 cell line showed little apoptotic changes.

Introduction

Tricarbonyl rhenium(I) complexes are being utilized more frequently because of the beneficial traits of the species such as structural diversity, rich spectroscopic properties, high stability, low toxicity as well as different modes of action making them prospective anticancer treatments that may be suitable for clinical study and development.[1] The MLCT bands, which start from the lowest triplet excited states as a result of the rapid vibrational relaxation and the intersystem crossing from the upper vibrational levels, are what give *fac*-[ReX(N–N)(CO)$_3$]$^{0/+}$ compounds (N–N: *N*,*N*-bidentate ligand, X = monodentate ligand) their luminous features with significant photophysical features *e.g.*, high Stokes shifts, long lifetimes, and strong quantum yields.[2] These benefits make it simple to distinguish between their emission and intervening autofluorescence.[3] The nature of the bidentate ligand and/or the auxiliary "spectator" ligand affects the photophysical features of this class of Re(I) compounds.[4–6] Re(I) complexes can regularly be followed intracellularly due to their luminous characteristics, allowing researchers to link their distribution inside cells and tissues to their method of action.[7–9] A few Re(I) complexes are reportedly promising therapeutics for the photodynamic treatment and/or photoactivated chemotherapy.[8,10,11]

Recent reviews[2,12–15] have covered the cytotoxicity of Re(I) complexes in detail, and it is clear from these that, with some exceptions, the cytotoxicity of Re(I) tricarbonyl complexes is often observed to increase with lipophilicity[16,17] (perhaps because of enhanced cellular uptake). A search in the literature shows that the majority of the anticancer activity of tricarbonyl Re(I) complexes have been focused on antiproliferative effects on the breast,[18–20] ovarian,[21,22] colon,[1,19,23–27] and epithelial adenocarcinoma.[17,28,29] Several studies have demonstrated that Re(I) complexes can have an anticancer effect by interfering with DNA,[30] preventing the activity of enzymes and protein kinases,[24,31] causing mitochondrial activity to be disrupted,[20,32,33] inducing cytoplasmic vacuolization,[34] and inducing apoptosis.[32,33] However, the mechanisms of action of these anticancer Re(I) complexes are still unknown, and little is known about their *in vivo* antitumor efficacy.

The benzimidazole scaffold is an interesting structural motif used in the context of several applications. For example, the chelating benzimidazole ligands have recently received a great deal of attention in the context of modelling biological systems due to the coordination chemistry of azoles serving as ligands in transition metal compounds.[35] In addition to its rich coordination chemistry, metal complexes with benzimidazole ligands have a number of possible applications, ranging from disciplines like liquid crystals and corrosion inhibition to different biological functions (antitumor,[36–38] antibacterial,[39–42] DNA-intercalating,[39,41] and anthelmintic[43]).

[a]*Department of Chemistry, Faculty of Science, Cairo University, Gamma Street, Giza, Cairo 12613, Egypt. E-mail: mansour@sci.cu.edu.eg; inorganic_am@yahoo.com*

[b]*Cancer Biology and Genetics Laboratory, Centre of Excellence for Advanced Sciences, National Research Centre, Dokki, Cairo 12622, Egypt*

[c]*Biochemistry Department, Biotechnology Research Institute, National Research Centre, Dokki, Cairo 12622, Egypt*

† Electronic supplementary information (ESI) available. See DOI: https://doi.org/10.1039/d2ra05992d

We synthesized two *fac*-Re(CO)$_3$ complexes functionalized with *N*,*N*-benzimidazole ligands (Scheme 1) in response to the intriguing antiproliferative effects and photophysical features of Re(I) complexes featuring some heterocyclic compounds. To learn more about the origin of the noted electronic transitions, simulations based on time-dependent density functional theory (TDDFT) were used. Besides, to gain an understanding of the nature of the lowest energy transitions, electronic absorption spectra were taken in solvents with varied polarities and hydrogen-bond types, and their solvatochromic characteristics were examined. A screen for the cytotoxicity of the two Re(I) complexes was performed against the human epithelial mammary gland breast adenocarcinoma (MCF7), human epithelial-like hepatocellular carcinoma (HepG2), and human epithelial colorectal adenocarcinoma (Caco-2) cell lines. The cytotoxicity results were compared to those observed in the normal mice splenocytes. Additionally, to shed light on their biotargets and methods of action, we examined the cellular localization of the rhenium(I) compounds by the aid of their autofluorescence using fluorescence microscopy. Moreover, the mode of cell death using acridine orange/ethidium bromide stain and the DNA fragmentation detection using TUNEL assay have been done to trace the effect of the Re(I) compounds on the cells and to figure out the prevailing mode of cell death and the effect on the DNA.

Results and discussion

Synthesis and characterization

The 1*H*-benzimidazol-2-ylmethyl-(*N*-aryl)amine derivatives (**1** and **2**) (Scheme 1) were made using a two-step technique described in the literature.[44–46] First, *o*-phenylenediamine was reacted with chloroacetic acid in 4 N HCl$_{(aq)}$ to produce 2-chloro methylbenzimidazole, which was then condensed with 4-chloro aniline and methyl-4-aminobenzoate in ethanol in presence of a small quantity of sodium iodide. In the absence of light, bromo tricarbonyl Re(I) complexes (**3** and **4**) were made by reacting ligands (**1** and **2**) with [ReBr(CO)$_5$] (Scheme 1). The yield and purity of the Re(I) complexes were good (54% (**3**), and 59% (**4**)). The complexes were fully characterized by elemental analysis, IR (Fig. S1†), NMR (^{1}H, and ^{13}C{^{1}H}), (Fig. S2–S5†), and ESI-MS. The IR spectra of **3** and **4** show two intense ν(C≡O) vibrations at (2018, 1892) and (2021, 1889) cm^{-1} assigned to the symmetrical and two overlapped anti-symmetrical stretching modes of the Re(CO)$_3$ moiety, respectively. The electrospray ionization mass spectra of **3** and **4**, in the positive mode, show a fragment at *m*/*z* 528.20 and 552.24 corresponding to {M − Br}$^+$ (M = molecular formula), respectively. Besides, unique fragment that matches {M − H − Br + K}$^+$ is observed in the mass spectra of **3** and **4** at *m*/*z* 567.23 and 591.30 in that order. Because the two protons are no longer isochronous, the methylene group of Re(I) complexes shows up as two quartets at (5.37, 5.07) and (5.41, 5.16) ppm (Fig. S2 & S3†). This could be explained by the two C–H bonds' varying polarisation, which is enhanced in polar solvents like acetone and results in the deshielding of the equatorial proton. Besides, the ^{1}H NMR spectra of **3**and **4** are characterized by two singlet NH signals at around 12.60 and 7.22 ppm (observed only in the case of **3**) for benzimidazolic and aniline residue NH groups, respectively. The ^{13}C NMR spectrum of **3** showed three CO signals at 196.6, 196.6, and 191.0 ppm (Fig. S4†).

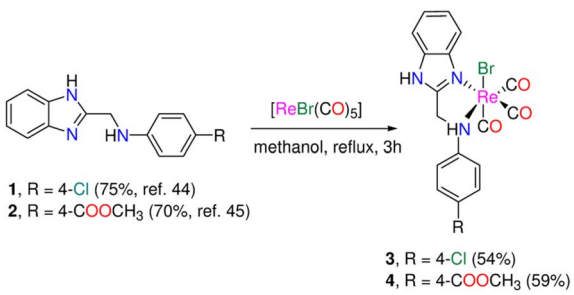

Scheme 1 Synthesis of tricarbonyl rhenium(I) complexes functionalized with *N*,*N*-bidentate benzimidazole ligands.

Absorption spectroscopy and TDDFT calculations

Changes in polarity across the phospholipid membrane have a role in the regulation of biological processes like permeability and the energetics of protein insertion. For a particular molecule, variations in the absorption or emission maxima can also result from environmental polarity. The term for this is solvatochromism.[5,47] The overall impact of the solvent on a particular species may also be influenced by other elements, such as interactions *via* hydrogen bonds. Compared to π–π* transitions, charge transfer bands (LLCT, MLCT) are more sensitive to solvent polarity. The significant difference in dipole moment between the ground state and stimulated state makes the CT bands easier to distinguish. Using a variety of solvents with wide-ranging polarities and coordinating abilities (DMSO, DMF, acetonitrile, 1,4-dioxane, tetrahydrofuran, dichloromethane, and toluene), the solvatochromic behaviours of **3** and **4** were investigated by UV/vis. spectroscopy. Except for DMF and DMSO, compound **3** is poorly soluble in all the tested solvents (Fig. S6†). In dichloromethane, the electronic absorption spectrum of **3** (Fig. S7†) shows five electronic transitions at 229, 276, 283, 336, and 432 nm. The band at 229 nm may be assigned to the low energy π–π* transition within the phenyl moiety.[45] The tautomeric structure of the benzimidazole ring gives rise to the two bands at 276 and 283 nm.[44] The transitions at 336 and 432 nm may be assigned to MLCT from Re(I) to benzimidazole moiety and CO ligands. The latter mentioned MLCT transitions are observed at (347, 425) and (340, 419) nm in 1,4-dioxane and THF, respectively. In general, when the solvent polarity was changed, there was no discernible spectrum shift in the lowest energy transition of compound **3**. The exchange of the axial Br$^-$ ligand with the coordinating solvents may be responsible for the non-systematic variation in the position of the MLCT bands. The exchange process is delayed when highly nonpolar solvents are present. The Br$^-$ exchange mechanism and the solvent's polarity impact seem to work differently. Once more, complex **4** has poor solubility in most of the organic solvents. Complex **4** is insoluble in toluene. Similar to the situation of **3**, the electronic

absorption spectrum of **4** in dichloromethane (Fig. S8†) exhibits five transitions at 233, 274, 282, 361, and 431 nm. Although there is a major red shift when switching from non-polar solvents to highly polar solvents like DMF (375 nm) and DMSO (377 nm) (Fig. 1), the effect of the solvent's polarity on the location of the band at 361 nm, in the case of dichloromethane, is systematic except for THF. The shifts in absorption maxima that have been observed are due to positive solvatochromism.[48,49]

TDDFT calculations were carried out in the singlet state using a Becke 3-parameter (exchange) Lee–Yang–Parr functional[50,51] (or hybrid exchange–correlation functional CAM-B3LYP, with a long-range correction term[52]) with LANL2DZ basis set,[53,54] and SMD solvation model[55] to get insight into the nature of the observed electronic transitions seen in the absorption spectra of **3** and **4**. The models that represented the suggested structures of our Re(I) complexes were first subjected to full-ground state geometry optimizations. The absence of fictitious vibrations suggests that the resulting geometries (Fig. 2) represent the complexes' local minimum structures. The atomic coordinates of the optimized structures and rotational constants are given in Tables S1 and S2.† Selected calculated bond lengths are given in Table S3.† The typical lengths and angles of the bonds in the two Re(I) derivatives show the little impact of the *para* substituent on the aniline ring on the chemical structural of the complexes.

The calculations for the TDDFT took into account the first 30 singlet excited states. The computed electronic spectra, the assigned electronic transitions, and their energies are given in Fig. S9, S10, and Table S4.† The absorption spectra of **3** and **4** were simulated by GAUSS-SUM software. A Gaussian convolution with a full width at half-maximum (FWHM) of 3000 cm^{-1} was used to interpolate each excited state. The TDDFT spectrum of **3**, obtained by B3LYP/LANL2DZ method, is characterized by three bands at 291, 448 and 569 nm equivalent to HOMO(α) → LUMO+1(α), HOMO(β) → LUMO(β) and HOMO−2(β) → LUMO(β), respectively. The reversed order may be due to HOMO experiencing a smaller solvent shift than most of the others.[56] As shown in Fig. 3, HOMO(β) has primarily p(Br)/d(Re)/π(CO) character, HOMO−2 has d(Re)/π(CO) character, whereas LUMO has π*(aniline moiety). As a result, the transitions at 448 and 569 nm are assigned to MLCT/LLCT in agreement with the

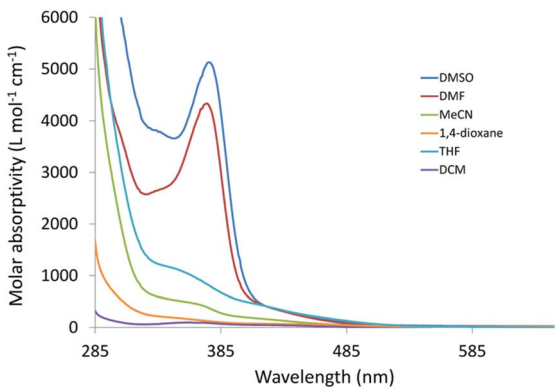

Fig. 1 Electronic absorption spectra of **4** in different solvents.

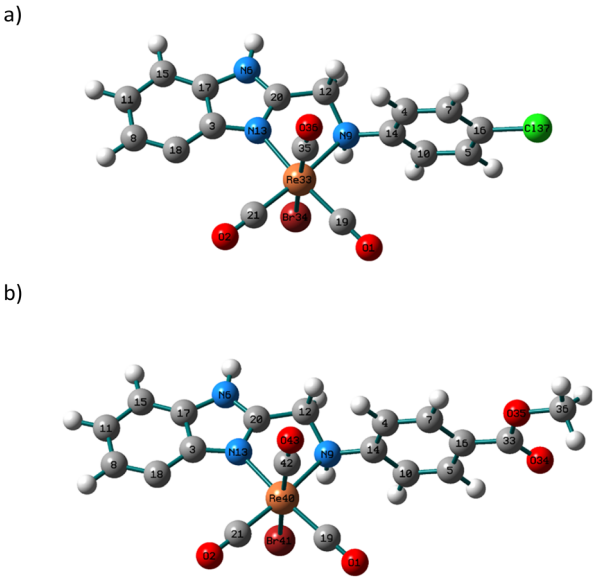

Fig. 2 Local minimum structures of tricarbonyl Re(I) complexes (a) **3** and (b) **4**.

experimental findings. Like **3**, the calculated spectrum of **4** has three bands at 294, 482, and 571 nm. The description of the frontier molecular orbitals of **4** and the assignment of the latter-mentioned electronic transitions (Table S5†) are comparable to those of complex **3**.

When compared to the other calculating method, B3LYP, CAM-B3LYP hybrid exchange-correlation functional, with a long-range correction term, has been shown to successfully predict the molecular charge transfer transitions. The spectrum of complex **3** generated by CAM-B3LYP functional is similar to that of B3LYP, although the bands are more pronounced at

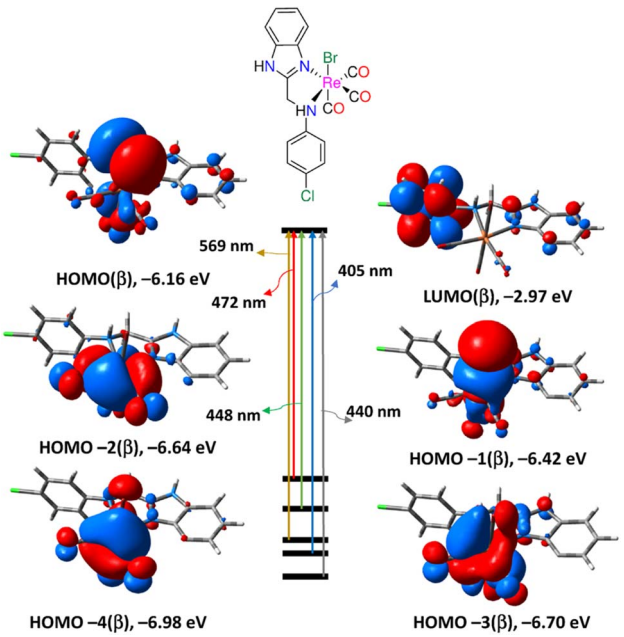

Fig. 3 Selected electronic transitions and frontier molecular orbitals of **3** calculated at B3LYP/LANL2DZ/SMD levels of theory.

shorter wavelengths. The main transitions are found at 285, 310, and 497 nm relating to HOMO−2(β) → LUMO(β), HOMO(β) → LUMO+1(β)/HOMO(α) → LUMO(α) and HOMO/HOMO−2(β) → LUMO(β), respectively. Similar to the B3LYP method, the lowest energy transition at 497 nm is assigned to MLCT initiating from d(Re) and terminating at aniline residue. Similar, the CAM-B3LYP spectrum of **4** has three main transitions at 289, 312 and 489 nm equivalent to HOMO−2(β) → LUMO(β), HOMO(β) → LUMO+2(β) and HOMO−3(β) → LUMO(β), in that order. Like **3**, the transition at 489 nm in the spectrum of **4** has an MLCT nature. Complex **4** is characterized by an electronic transition at 381 nm (HOMO−4(β) → LUMO(β)), matching the experimental one at around 377 nm (in DMSO), and it is assigned to MLCT.

Natural bond orbital analyses

From the natural bond orbital (NBO) analysis of Weinhold and co-workers[57] and the second order perturbation theory analysis of Fock Matrix in NBO Basis produced at B3LYP/LANL2DZ level of theory, it was possible to infer the natural charge, nature of bonding, type of hybridization, and strength of the bonds (M–N, M–C, and M–Br) of the local minimum structures of complexes **3** and **4**. The natural charge and the electronic arrangement of rhenium ion in **3** are −0.93590*e* and [Xe]$6s^{0.42}5d^{6.69}6p^{0.85}6d^{0.02}$. The occupancies of the 5d-orbitals are as follows: $d_{xy}^{1.09356}d_{xz}^{1.38835}d_{yz}^{1.37005}d_{x^2-y^2}^{1.56678}d_{z^2}^{1.26835}$. The σ(Re–C19) bond is formed from $sp^{0.71}d^{2.46}$ hybrid on the Re atom (a mixture of 23.98% s, 16.95% p, and 59.07% d) and $sp^{0.51}$ hybrid on C19 (a mixture of 66.03% s, and 33.97% p) and is polarized towards C19 atom (62.38%). The other σ(Re–C21) and σ(Re–C35) bonds are polarised toward carbon atoms with values of 61.29% and 63.04%, respectively, and exhibit hybridizations that are identical to those of σ(Re–C19). The σ(Re–Br) bond is created from $sp^{5.52}d^{3.49}$ hybrid on the Re atom (comprised of 9.99% s, 55.18% p, and 34.83% d) and $sp^{4.10}$ hybrid on Br (a mixture of 19.62% s, and 80.38% p) and is polarized towards Br atom (76.09%). Through a lone pair interaction, the two nitrogen atoms of the benzimidazole ligand bind the metal centre. The NBO analyses of **4** and the hybridization of Re–L bonds are typical to those of **3**.

Hyper-conjugation is described as a stabilizing effect that results from the overlap of two electron-deficient orbitals, one of which is occupied. From the second-order perturbation method of the Fock Matrix in NBO basis between donor–acceptor orbitals, the hyper-conjugative interaction energy was calculated. The intensity of the interaction between electron donors and electron acceptors, or the degree to which electron donors are inclined to donate to electron acceptors, increases with the second-order interaction energy (E^2) value. Finding a rise in the electron density (ED) of the anti-bonding orbital that weakens the corresponding bonds might help identify these interactions. For **3**, the E^2 values of σ(Re–C19)→, σ(Re–C21)→, σ(Re–C35)→, σ(Re–Br)→, LP(1)N9→, and LP(1)N13 → σ*(Re–C19) are 0.80, 7.08, 4.10, 0.92, 0.66 and 12.91 kcal mol^{-1}, respectively. The strongest value demonstrates how the secondary amino group plays a role in regulating the stability of this class of Re(I) complexes. It occurs when N13 interacts with σ*(Re–C19). In the case of **4**, the E^2 values of σ(Re–C19)→, σ(Re–C21)→, σ(Re–C42)→, σ(Re–Br)→, LP(1)N9→, and LP(1)N13 → σ*(Re–C19) are 0.80, 7.10, 0.92, 4.06, 0.65 and 12.93 kcal mol^{-1}, respectively. In comparison, it seems that the changing nature of the *para*-substituted on the aniline has little effect on the stability of this class of complexes.

Cell viability assay

We next aimed to assess the *in vitro* anticancer activity of the Re(I) benzimidazole complexes after thoroughly examining their physicochemical characteristics. Cell cultures of HepG2, MCF7, Caco-2, and normal splenocytes were incubated with the complexes at various concentrations (from 6.25 to 200 μg mL^{-1}) in the dark for 18 h in order to assess the differential cytotoxicity of the synthesized complexes. The cytotoxicity was assessed using the colorimetric MTT assay. The concentration needed to inhibit 50% of the cell proliferation (IC_{50} value) was determined for the tested complexes (Fig. S11†). Each sample's cytotoxic effect on the various cell lines under study varied. In contrast to compound **4**, which is completely safe for normal splenocytes, complex **3** had minor toxicity of up to 25%. Our Re(I) complexes had only marginally cytotoxic effects on the tested malignant cells with IC_{50} not less than 90 μg mL^{-1} on all cell lines (Table S6†) when compared to those reported in the literature with some nitrogen donor ligands.[12,14]

The mode of cell death

The acridine orange/ethidium bromide stain recognizes the mode of cell death. The early and late apoptotic in addition to the necrotic cells are made visible by the exclusion dye, ethidium bromide, which binds to the DNA of the membrane-damaged cells. Early, and late apoptotic as well as necrotic cell types are identified by their different hues of yellowish green, yellowish orange, and orange to red. The MCF-7 cell line was selectively affected by both Re(I) complexes. The Caco-2 cell line was moderately affected by the tested compounds, while the least affected cell line was the HepG2. The mode of cell death of all compounds is shown in Fig. 4.

Autofluorescence of Re(I) compounds and their positioning within the cells

The two rhenium(I) complexes have a strong autofluorescence emission in the range of 460–488 nm. They appear under the fluorescent microscope, without the aid of any dye, as strong, reddish-colored compounds. They appear to accumulate around the cellular membranes and within the intercellular junctions (Fig. 5). The photos revealed that the compounds are collected along the cell membrane waiting for their entry. The photos also showed the entry of the compounds, and their presence within the cytoplasm of the cells in very fine cytoplasmic accumulations.

The DNA fragmentation (TUNEL assay)

Visualization of the DNA damage and DNA fragmentation were performed by using the *in situ* BrdU-Red DNA fragmentation kit.

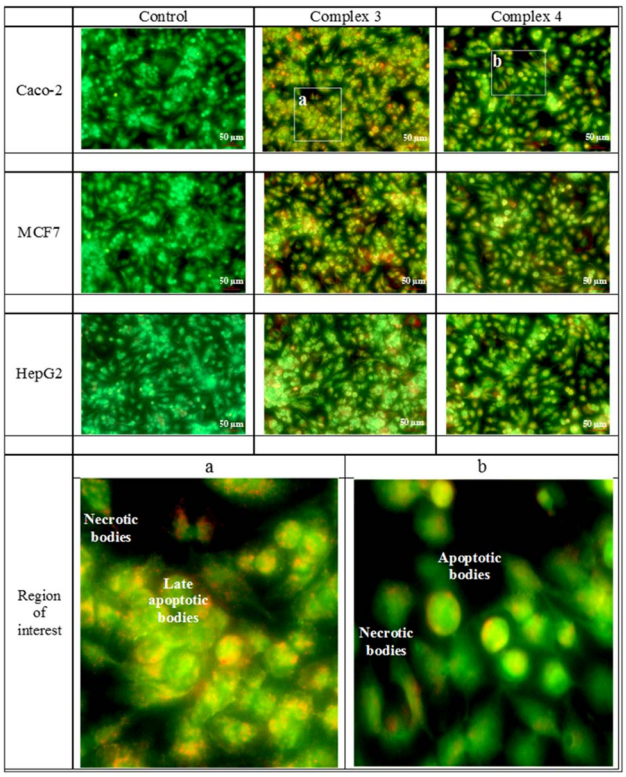

Fig. 4 The mode of cell death using acridine orange/ethidium bromide stain. Complex **3** shows increased apoptotic changes in the MCF-7, and the Caco-2 cell lines, while the HepG2 cell line shows little apoptotic changes. Compound **4** shows little apoptotic changes and very minute necrotic changes. Two examples from the photos are enlarged to show the apoptotic and necrotic bodies. The magnification 20X. The scale bar 50 μm.

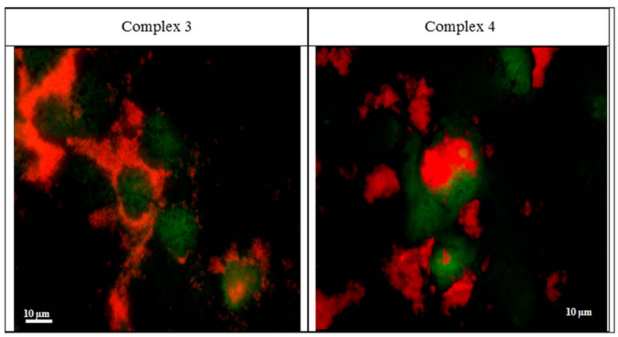

Fig. 5 The autofluorescence of the rhenium samples and their positioning within the cells. In both complexes, the compounds are accumulated around the cellular membranes as a step before entering the cells. The compounds are also seen within the cytosol of the cells in minute particles. In compound **3**, it is seen in the intercellular junction. The magnification 100X. The scale bar 10 μm.

It allows the terminal deoxynucleotidyl transferase (TdT) to catalyse the insertion of bromolated deoxyuridine triphosphate nucleotide (BrdUTP) at the free 3′-hydroxyl ends of the fragmented DNA. The greater the DNA fragmentation, the greater the insertion of BrdUTP, the more TUNEL positive cells. The Re(I) complexes appeared to cause DNA fragmentations in all

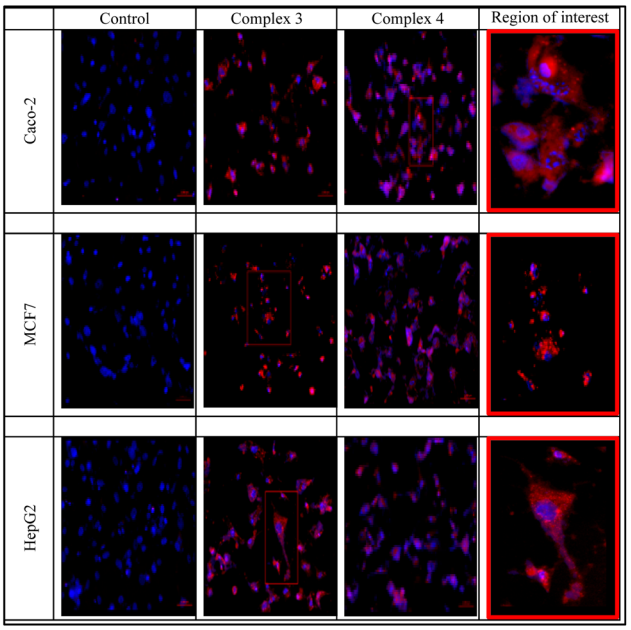

Fig. 6 The TUNEL results of the rhenium complexes in comparison to the control groups. Both complexes show high DNA fragmentation with the very increased incorporation of the BrdU-Red in the fragmented DNA. The zoomed photos show the position of fragmentation around the nuclei and the blue DAPI shows the fragmented nuclear bodies as well. The magnification 20X. The scale bar 50 μm.

cell lines especially complex **4.** The DNA specific dye (DAPI) also showed fragmented nuclear bodies in many cells denoting the initiation of apoptosis in many cells. The TUNEL positive cells are shown in Fig. 6 and S12–S14.†

Conclusion

In response to the fascinating antiproliferative properties and photophysical characteristics of rhenium(I) complexes including certain heterocyclic molecules, we provided two *fac*-$Re(CO)_3$ complexes functionalized with *N*,*N*-benzimidazole ligands. After carefully evaluating the physicochemical properties of the Re(I) benzimidazole complexes, our next goal was to evaluate the *in vitro* anticancer efficacy of these compounds against three malignant and one normal cell lines of different origins. On all cell lines evaluated, the IC_{50} of our Re(I) complexes was greater than 90 μg mL^{-1}, indicating only moderate cytotoxicity against the malignant cells. Complex **4**, functionalized with methyl ester group is completely safe for normal splenocytes, while the other complex **3**, which is decorated with chloro group, had minor toxicity up to 25%. Our Re(I) derivatives have a significant autofluorescence emission in the region of 460–488 nm without the use of any dyes, which is their principal benefit. Re(I) complexes build up around cellular membranes and within intercellular connections as they wait to enter, as evidenced by the fluorescent microscopy. The images also demonstrated the chemicals' entrance into the cells' cytoplasm and their existence there in extremely small cytoplasmic accumulations. The two complexes caused increased early and late apoptotic changes in addition to valuable necrotic levels

denoted by the acridine orange/ethidium bromide staining. This was also assured by the increased number of TUNEL positive DNA fragmented cells. Complex **3** was more toxic to the Caco-2 cell line than the MCF7 and HepG2 cell lines, with the lowest IC_{50} and highest apoptosis/necrosis percentage. In comparison to complex **3**, complex **4** induced more DNA fragments in the Caco-2 cell line. The observation that the complex is piled in and around the cellular membranes as well as in the intercellular gaps, leads to DNA fragments and damage. This ultimately caused apoptosis and clearly visible necrosis in the cells.

Experimental section

Materials and instruments

The previously described procedure was used to synthesize 2-chloromethylbenzimidazole,[44] by heating to reflux a mixture of *o*-phenylenediamine and chloroacetic acid in 4 N hydrochloric acid. 1*H*-Benzimidazol-2-ylmethyl-(*N*-phenyl)amine derivatives (**1** and **2**) were prepared using the instructions that were published.[45,46] The chemicals, which included the organic solvents, were bought from reputable commercial suppliers and utilized exactly as directed. On a Bruker Alpha-E instrument, ATR-IR spectra of solid-state tricarbonyl Re(I) complexes (**3** and **4**) were recorded. Using a Specord 200 Plus spectrophotometer, the solvatochromism characteristics were measured. Using the Automatic Analyzer CHNS, Vario EL III Elementar, the CHN elemental analyses of the novel complexes were quantified. On the Advion compact mass spectrometer, mass spectra were captured. A Bruker-Advance 400 spectrometer was used to record the ^{1}H and ^{13}C{^{1}H} NMR resonances (^{1}H, 400.40 MHz; ^{13}C{^{1}H}, 100.70 MHz).

Synthesis of tricarbonyl Re(I) complexes

To a round-bottomed flask charged with [$ReBr(CO)_5$] (50 mg, 0.123 mmol), and methanol (20 mL), 1*H*-benzimidazol-2-ylmethyl-(*N*-aryl)amine derivatives [0.123 mmol; **1**, 35 mg; **2**, 31 mg] was added. The reaction mixture was heated to reflux for 3 h. As the reaction solvent evaporated, yellow powders developed, which were then dried under vacuum after being washed with diethyl ether (3 × 5 mL).

[$ReBr(CO)_3L^{Cl}$] (**3**): yield: 54% (44 mg, 0.072 mmol). IR (ATR): ν = 3200 (w, NH), 2018 (vs, C≡O), 1892 (vs, C≡O), 1473, 1434, 1201, 1060, 999, 947 cm^{-1}. ^{1}H NMR (400.40 MHz, acetone-d_6): δ = 12.62 (s, 1H, bim-NH), 7.79 (d, 1H, $^3J_{H,H}$ = 7.82 Hz, bim-H7), 7.73 (d, 1H, $^3J_{H,H}$ = 7.83 Hz, bim-H4), 7.49 (m, 4H, bim-H5/H6/phenyl-H2/H6), 7.42 (d, 2H, $^3J_{H,H}$ = 9.41 Hz, phenyl-H3/H5), 7.22 (t, 1H, $^3J_{H,H}$ = 5.21 Hz, NH), (5.37, 5.07) (m, 2H, CH_2) ppm. ^{13}C NMR (100.10 MHz, acetone-d_6): δ = 196.9 (C≡O), 196.6 (C≡O), 191.0 (C≡O), 157.6, 149.0, 140.8, 134.0, 130.3, 129.4, 129.1, 124.7, 124.0, 122.8, 120.9, 118.0, 112.8, 51.5 (CH_2) ppm. ESI-MS (positive mode, acetone): m/z = 528.20 {M − Br}$^+$ (M = molecular formula) and 567.23 {M − H − Br + K}$^+$. $C_{17}H_{12}N_3O_3ClBrRe$: C 33.59, H 1.99, N 6.91; found C 33.37, H 2.58, N 7.17.

[$ReBr(CO)_3L^{COOCH_3}$] (**4**): yield: 59% (42 mg, 0.067 mmol). IR (ATR): ν = 3182 (w, NH), 2021 (vs, C≡O), 1889 (vs, C≡O), 1698, 1284, 1186, 1116, 1066, 934 cm^{-1}. ^{1}H NMR (400.40 MHz, acetone-d_6): δ = 12.64 (s, 1H, bim-NH), 8.09 (d, 2H, $^3J_{H,H}$ = 9.41 Hz, phenyl-H3/H5), 7.79 (d, 1H, $^3J_{H,H}$ = 7.94 Hz, bim-H4), 7.74 (d, 1H, $^3J_{H,H}$ = 7.33 Hz, bim-H7), 7.49 (m, 4H, bim-H5/H6/phenyl-H2/H6), (5.41, 5.16) (m, 2H, CH_2) and 3.89 (s, 3H, CH_3) ppm. ^{13}C NMR (100.10 MHz, acetone-d_6): δ = 166.1, 154.7, 141.5, 134.6, 131.7, 128.1, 125.4, 124.9, 121.7, 119.9, 118.7, 113.6, 113.5, 52.3 (CH_3), (51.7, 51.6) (CH_2) ppm. ESI-MS (positive mode, acetone): m/z = 552.24 {M − Br}$^+$ (M = molecular formula) and 591.30 {M − H − Br + K}$^+$. $C_{19}H_{15}N_3O_5BrRe\cdot 3H_2O$: C 33.29, H 3.09, N 6.13; found C 32.68, H 2.65, N 6.07.

Density functional theory calculations

Gaussian03 software[58] was used to carry out the geometry optimizations of functionalized *fac*-$Re(CO)_3$ compounds in the ground state, harmonic frequencies analyses, and TDDFT calculations. The local minimum structures were obtained using B3LYP functional,[50,51] and LANL2DZ basis set.[53,54] The Weinhold and Carpenter natural bond orbital (NBO) investigation has produced the net atomic charges.[57] The B3LYP/LANL2DZ and CAM-B3LYP[52]/LANL2DZ methods in combination with the SMD solvation model were used to perform TDDFT calculations in the singlet state. Visualization of electronic spectra and frontier molecular orbitals were made by Gaussview03.[59]

Cell viability assay

Cells. Human epithelial colorectal adenocarcinoma (Caco-2), human epithelial mammary gland breast adenocarcinoma (MCF7), and human epithelial-like hepatocellular carcinoma (HepG2) were purchased from ATCC, USA. In addition to mice adherent splenocytes which were obtained according to Han and co-workers' protocol with slight modifications[60] and after obtaining the approval of the ethical committee of the National Research Centre.

Cell culture. The RPMI-1640 medium was used for culturing the Caco-2, MCF7, and mice splenocytes. For the HepG2 cell line, cells were cultured in DMEM. All the media were supplemented with 10% fetal bovine serum (FBS), 2 mM L-glutamine, containing 100 units per mL penicillin G sodium, 100 units per mL streptomycin sulphate, and 250 ng per mL amphotericin B. All from Lonza (Basel, Switzerland). Cells were maintained at sub-confluency at 37 °C in humidified air containing 5% CO_2. For sub-culturing, monolayer cells were harvested after trypsin/EDTA treatment at 37 °C. Cells were used when confluence had reached 75%.

MTT cytotoxicity. 3-[4,5-Dimethylthiazole-2-yl]-2,5-diphenyltetrazolium bromide (MTT), obtained from Merck KGaA (Darmstadt, Germany). On the various cell lines, it is utilized to evaluate the cytotoxicity of the examined complexes. It is based on the idea that the ability of active mitochondrial dehydrogenase enzyme of alive cells to break the tetrazolium rings of the yellow MTT and generate dark blue insoluble formazan crystals directly proportional to the number of live cells.

In brief, cells (1×10^4 cells per well) were seeded in the corresponding medium of each cell line in a flat bottom 96-well microplate and treated with 20 μL of serial dilutions of the tested samples beginning with 200 μg mL^{-1} and ending with 6.25 μg mL^{-1}. The experiment was conducted for 24 h at 37 °C in a humidified 5% CO_2 atmosphere. The media were removed after incubation, followed by the addition of 40 μL of MTT solution per well and a further 4 h of incubation. The MTT crystals were dissolved by adding 180 μL of acidified isopropanol per well, and the plates were then shaken at room temperature. The absorbance at 570 nm was then determined photometrically using a microplate ELISA reader (FLUOstar OPTIMA, BMG LABTECH GmbH, Ortenberg, Germany). Three times repeats were performed for each concentration and the average was calculated.[61]

Mode of cell death. The cells were cultured on 8 well cell culture slides (SPL, Seoul, South Korea) at density 10^4 cells per well and the samples were adapted for a final concentration of 25% of each IC_{50} of each sample on the respective cell line. After 24 h of incubation, the mode of the cell death was examined in the cells after staining with acridine orange (100 μg mL^{-1}) and ethidium bromide (100 μg mL^{-1}) dual stain dissolved in phosphate buffer saline (PBS) at equal volume, all obtained from Merck KGaA (Darmstadt, Germany). The cells were stained before being examined under a fluorescence microscope (AxioImager Z2, Zeiss, Jena, Germany). Green-colored cells were classified as "living," whereas yellow, orange, or red cells were classified as "early apoptotic," "late apoptotic," or "necrotic," respectively.[62] Three separate experiments were conducted ($n = 3$).

DNA fragmentation detection (TUNEL assay). TUNEL (terminal deoxynucleotidyl transferase-mediated dUTP nick-end labeling) assay is used to detect the DNA fragmentation *in situ* using TUNEL assay kit-BrdU-Red (ab66110, abcam, Cambridge, UK). As previously noted, the cells were cultivated on cell culture slides. Following a 24 h incubation period, the cells were fixed with 4% paraformaldehyde, subjected to an hour-long incubation with DNA labeling solution, washed, and then subjected to a 30 min incubation with an antibody solution before being examined under a fluorescent microscope at Ex/Em 488/576 nm.

Autofluorescence of rhenium compounds. The cells were cultured on cell culture slides as mentioned above. The cells were extensively washed to remove any debris and the autofluorescence of the rhenium samples (**3** and **4**) was detected without the addition of any dye under the fluorescent microscope (AxioImager Z2) with a fluorescent camera (AxioCam MRc3 S/N 4299) and ZEN 11 blue edition software for Image Analysis. The instrument was purchased from Zeiss, Jena, Germany. The excitation wavelength was $\lambda = 460$–488 nm. The reflector was 62 HE BFP/GFP/HcRed.

Author contributions

Mansour and Abo-Elfadl: conceptualization, methodology, validation, supervision, investigation, writing – original draft and review. Farag: supervision, review & editing. Ibrahim: methodology.

Conflicts of interest

There are no conflicts to declare.

References

1 J. Delasoie, A. Pavic, N. Voutier, S. Vojnovic, A. Crochet, J. Nikodinovic-Runic and F. Zobi, Identification of novel potent and non-toxic anticancer, anti-angiogenic and antimetastatic rhenium complexes against colorectal carcinoma, *Eur. J. Med. Chem.*, 2020, **204**, 112583.
2 S. Hostachy, C. Policar and N. Delsuc, Re (I) carbonyl complexes: Multimodal platforms for inorganic chemical biology, *Coord. Chem. Rev.*, 2017, **351**, 172–188.
3 A. J. Amoroso, R. J. Arthur, M. P. Coogan, V. Fernández-Moreira, A. J. Hayes, D. Lloyd, C. Millet and S. J. Pope, 3-Chloromethylpyridyl bipyridine fac-tricarbonyl rhenium: a thiol-reactive luminophore for fluorescence microscopy accumulates in mitochondria, *New J. Chem.*, 2008, **32**(7), 1097–1102.
4 A. M. Mansour, Pyridylbenzimidazole based Re (I)(CO) 3 complexes: antimicrobial activity, spectroscopic and density functional theory calculations, *RSC Adv.*, 2019, **9**(26), 15108–15114.
5 A. M. Mansour, Tricarbonyl triazolato Re (i) compounds of pyridylbenzimidazole ligands: spectroscopic and antimicrobial activity evaluation, *RSC Adv.*, 2021, **11**(37), 22715–22722.
6 A. M. Mansour, K. Radacki and O. R. Shehab, Role of the ancillary ligand in controlling the lysozyme affinity and electronic properties of terpyridine fac-Re (CO) 3 complexes, *Dalton Trans.*, 2021, **50**(4), 1197–1201.
7 V. Fernández-Moreira, F. L. Thorp-Greenwood and M. P. Coogan, Application of d^6 transition metal complexes in fluorescence cell imaging, *Chem. Commun.*, 2010, **46**(2), 186–202.
8 A. Leonidova, V. Pierroz, R. Rubbiani, J. Heier, S. Ferrari and G. Gasser, Towards cancer cell-specific phototoxic organometallic rhenium (I) complexes, *Dalton Trans.*, 2014, **43**(11), 4287–4294.
9 K. K.-W. Lo, M.-W. Louie and K. Y. Zhang, Design of luminescent iridium(III) and rhenium(I) polypyridine complexes as *in vitro* and *in vivo* ion, molecular and biological probes, *Coord. Chem. Rev.*, 2010, **254**(21–22), 2603–2622.
10 K. Wähler, A. Ludewig, P. Szabo, K. Harms and E. Meggers, Rhenium Complexes with Red-Light-Induced Anticancer Activity, *Eur. J. Inorg. Chem.*, 2014, **2014**(5), 807–811.
11 S. C. Marker, S. N. MacMillan, W. R. Zipfel, Z. Li, P. C. Ford and J. J. Wilson, Photoactivated in vitro anticancer activity of rhenium (I) tricarbonyl complexes bearing water-soluble phosphines, *Inorg. Chem.*, 2018, **57**(3), 1311–1331.

12 A. Leonidova and G. Gasser, Underestimated potential of organometallic rhenium complexes as anticancer agents, *ACS Chem. Biol.*, 2014, **9**(10), 2180–2193.

13 K. K. W. Lo, K. Y. Zhang and S. P. Y. Li, Recent exploitation of luminescent rhenium (I) tricarbonyl polypyridine complexes as biomolecular and cellular probes, *Eur. J. Inorg. Chem.*, 2011, **2011**(24), 3551–3568.

14 E. B. Bauer, A. A. Haase, R. M. Reich, D. C. Crans and F. E. Kühn, Organometallic and coordination rhenium compounds and their potential in cancer therapy, *Coord. Chem. Rev.*, 2019, **393**, 79–117.

15 C. C. Konkankit, S. C. Marker, K. M. Knopf and J. J. Wilson, Anticancer activity of complexes of the third row transition metals, rhenium, osmium, and iridium, *Dalton Trans.*, 2018, **47**(30), 9934–9974.

16 A. J. Amoroso, M. P. Coogan, J. E. Dunne, V. Fernández-Moreira, J. B. Hess, A. J. Hayes, D. Lloyd, C. Millet, S. J. Pope and C. Williams, Rhenium fac tricarbonyl bisimine complexes: biologically useful fluorochromes for cell imaging applications, *Chem. Commun.*, 2007, (29), 3066–3068.

17 R. R. Ye, C. P. Tan, M. H. Chen, L. Hao, L. N. Ji and Z. W. Mao, Mono-and Dinuclear Phosphorescent Rhenium(I) Complexes: Impact of Subcellular Localization on Anticancer Mechanisms, *Chem.–Eur. J.*, 2016, **22**(23), 7800–7809.

18 N. A. Illán-Cabeza, A. R. García-García, M. N. Moreno-Carretero, J. M. Martínez-Martos and M. J. Ramírez-Expósito, Synthesis, characterization and antiproliferative behavior of tricarbonyl complexes of rhenium(I) with some 6-amino-5-nitrosouracil derivatives: crystal structure of fac-[$ReCl(CO)_3$(DANU-N5, O_4)](DANU= 6-amino-1, 3-dimethyl-5-nitrosouracil), *J. Inorg. Biochem.*, 2005, **99**(8), 1637–1645.

19 P. Collery, V. Veena, A. Harikrishnan and D. Desmaele, The rhenium (I)-diselenoether anticancer drug targets ROS, TGF-β1, VEGF-A, and IGF-1 in an in vitro experimental model of triple-negative breast cancers, *Invest. New Drugs*, 2019, **37**(5), 973–983.

20 I. Kitanovic, S. Can, H. Alborzinia, A. Kitanovic, V. Pierroz, A. Leonidova, A. Pinto, B. Spingler, S. Ferrari and R. Molteni, A deadly organometallic luminescent probe: anticancer activity of a ReI bisquinoline complex, *Chem.–Eur. J.*, 2014, **20**(9), 2496–2507.

21 C. C. Konkankit, A. P. King, K. M. Knopf, T. L. Southard and J. J. Wilson, In vivo anticancer activity of a rhenium (I) tricarbonyl complex, *ACS Med. Chem. Lett.*, 2019, **10**(5), 822–827.

22 C. C. Konkankit, B. A. Vaughn, S. N. MacMillan, E. Boros and J. J. Wilson, Combinatorial synthesis to identify a potent, necrosis-inducing rhenium anticancer agent, *Inorg. Chem.*, 2019, **58**(6), 3895–3909.

23 A. Kermagoret, G. Morgant, J. d'Angelo, A. Tomas, P. Roussel, G. Bastian, P. Collery and D. Desmaële, Synthesis, structural characterization and biological activity against several human tumor cell lines of four rhenium (I) diseleno-ethers complexes: $Re(CO)_3Cl$ ($PhSe(CH_2)_2SePh$), $Re(CO)_3Cl$ ($PhSe(CH_2)_3SePh$), $Re(CO)_3Cl$ (HO2C–CH2Se (CH2) 2SeCH2–CO2H) and $Re(CO)_3Cl$ (HO2C–CH2Se (CH2) 3SeCH2–CO2H), *Polyhedron*, 2011, **30**(2), 347–353.

24 M. Muñoz-Osses, F. Godoy, A. Fierro, A. Gómez and N. Metzler-Nolte, New organometallic imines of rhenium (i) as potential ligands of GSK-3β: synthesis, characterization and biological studies, *Dalton Trans.*, 2018, **47**(4), 1233–1242.

25 M. Muñoz-Osses, D. Siegmund, A. Gómez, F. Godoy, A. Fierro, L. Llanos, D. Aravena and N. Metzler-Nolte, Influence of the substituent on the phosphine ligand in novel rhenium (i) aldehydes. Synthesis, computational studies and first insights into the antiproliferative activity, *Dalton Trans.*, 2018, **47**(39), 13861–13869.

26 C. A. Kumar, R. Nagarajaprakash, W. Victoria, V. Veena, N. Sakthivel and B. Manimaran, Synthesis, characterisation and cytotoxicity studies of manganese (I) and rhenium (I) based metallacrown ethers, *Inorg. Chem. Commun.*, 2016, **64**, 39–44.

27 R. Huang, G. Langille, R. K. Gill, C. M. J. Li, Y. Mikata, M. Q. Wong, D. T. Yapp and T. Storr, Synthesis, characterization, and biological studies of emissive rhenium–glutamine conjugates, *JBIC, J. Biol. Inorg. Chem.*, 2013, **18**(7), 831–844.

28 J. Yang, J.-X. Zhao, Q. Cao, L. Hao, D. Zhou, Z. Gan, L.-N. Ji and Z.-W. Mao, Simultaneously inducing and tracking cancer cell metabolism repression by mitochondria-immobilized rhenium (I) complex, *ACS Appl. Mater. Interfaces*, 2017, **9**(16), 13900–13912.

29 L. He, Z.-Y. Pan, W.-W. Qin, Y. Li, C.-P. Tan and Z.-W. Mao, Impairment of the autophagy-related lysosomal degradation pathway by an anticancer rhenium (i) complex, *Dalton Trans.*, 2019, **48**(13), 4398–4404.

30 D.-L. Ma, C.-M. Che, F.-M. Siu, M. Yang and K.-Y. Wong, DNA binding and cytotoxicity of ruthenium(II) and rhenium(I) complexes of 2-amino-4-phenylamino-6-(2-pyridyl)-1, 3, 5-triazine, *Inorg. Chem.*, 2007, **46**(3), 740–749.

31 P. V. Simpson, I. Casari, S. Paternoster, B. W. Skelton, M. Falasca and M. Massi, Defining the anti-cancer activity of tricarbonyl rhenium complexes: induction of G2/M cell cycle arrest and blockade of Aurora-A kinase phosphorylation, *Chem.–Eur. J.*, 2017, **23**(27), 6518–6521.

32 S. Imstepf, V. Pierroz, R. Rubbiani, M. Felber, T. Fox, G. Gasser and R. Alberto, Organometallic rhenium complexes divert doxorubicin to the mitochondria, *Angew. Chem.*, 2016, **128**(8), 2842–2845.

33 M. König, D. Siegmund, L. J. Raszeja, A. Prokop and N. Metzler-Nolte, Resistance-breaking profiling and gene expression analysis on an organometallic Re I–phenanthridine complex reveal parallel activation of two apoptotic pathways, *MedChemComm*, 2018, **9**(1), 173–180.

34 K. M. Knopf, B. L. Murphy, S. N. MacMillan, J. M. Baskin, M. P. Barr, E. Boros and J. J. Wilson, In vitro anticancer activity and *in vivo* biodistribution of rhenium (I) tricarbonyl aqua complexes, *J. Am. Chem. Soc.*, 2017, **139**(40), 14302–14314.

35 E. Bouwman, W. Driessen and J. Reedijk, Model systems for type I copper proteins: structures of copper coordination compounds with thioether and azole-containing ligands, *Coord. Chem. Rev.*, 1990, **104**(1), 143–172.

36 N. T. A. Ghani and A. M. Mansour, Novel palladium(II) and platinum(II) complexes with 1H-benzimidazol-2-ylmethyl-N-(4-bromo-phenyl)-amine: Structural studies and anticancer activity, *Eur. J. Med. Chem.*, 2012, **47**, 399–411.

37 A. M. Mansour and N. T. Abdel-Ghani, Synthesis, spectroscopic, DFT, cytotoxicity and antimicrobial activity of Pd (II) and Pt (II) complexes of N, N-chelated benzimidazole derivatives, *Inorg. Chim. Acta*, 2015, **438**, 76–84.

38 F. Gümüş, Ö. Algül, G. Eren, H. Eroğlu, N. Diril, S. Gür and A. Özkul, Synthesis, cytotoxic activity on MCF-7 cell line and mutagenic activity of platinum(II) complexes with 2-substituted benzimidazole ligands, *Eur. J. Med. Chem.*, 2003, **38**(5), 473–480.

39 A. M. Mansour and O. R. Shehab, Lysozyme and DNA binding affinity of Pd (II) and Pt (II) complexes bearing charged N, N-pyridylbenzimidazole bidentate ligands, *Dalton Trans.*, 2018, **47**(10), 3459–3468.

40 A. M. Mansour and O. R. Shehab, Pyridylbenzimidazole-Based Gold (III) Complexes: Lysozyme Metalation, DNA Binding Studies, and Biological Activity, *Eur. J. Inorg. Chem.*, 2019, **2019**(23), 2830–2838.

41 A. M. Mansour and K. Radacki, Antimicrobial properties of half-sandwich Ir (III) cyclopentadienyl complexes with pyridylbenzimidazole ligands, *Dalton Trans.*, 2020, **49**(14), 4491–4501.

42 A. M. Mansour, K. Radacki and O. R. Shehab, Role of the ancillary ligand in determining the antimicrobial activity of Pd (II) complexes with N^ N^ N-tridentate coligand, *Polyhedron*, 2022, **221**, 115857.

43 D. Hernández-Romero, S. Rosete-Luna, A. López-Monteon, A. Chávez-Piña, N. Pérez-Hernández, J. Marroquín-Flores, A. Cruz-Navarro, G. Pesado-Gómez, D. Morales-Morales and R. Colorado-Peralta, First-row transition metal compounds containing benzimidazole ligands: An overview of their anticancer and antitumor activity, *Coord. Chem. Rev.*, 2021, **439**, 213930.

44 N. T. A. Ghani and A. M. Mansour, Molecular structure of 2-chloromethyl-1H-benzimidazole hydrochloride: Single crystal, spectral, biological studies, and DFT calculations, *Spectrochim. Acta, Part A*, 2012, **86**, 605–613.

45 N. T. A. Ghani and A. M. Mansour, Molecular structures of 2-arylaminomethyl-1H-benzimidazole: spectral, electrochemical, DFT and biological studies, *Spectrochim. Acta, Part A*, 2012, **91**, 272–284.

46 A. M. Mansour, C. Steiger, C. Nagel and U. Schatzschneider, Wavelength-dependent control of the CO release kinetics of manganese (I) tricarbonyl PhotoCORMs with benzimidazole coligands, *Eur. J. Inorg. Chem.*, 2019, **2019**(42), 4572–4581.

47 E. G. Randles and P. R. Bergethon, Environment Reaction Fields for Lipophilic Fluorophores using Solvatochromic Shifts, *Biophys. J.*, 2013, **104**(2), 83a.

48 Y. Li, Z. Y. Lin and W. T. Wong, Synthesis, Structural Characterization, Solvatochromism, and Electrochemistry of Tetra-Osmium Carbonyl Clusters Containing Azo-Ligands, *Eur. J. Inorg. Chem.*, 2001, **2001**(12), 3163–3173.

49 N. M. Ibrahim, R. M. Khaled, M. A. Ragheb, K. Radacki, A. M. Farag and A. M. Mansour, Light-activated cytotoxicity of dicarbonyl Ru (II) complexes with a benzimidazole coligand towards breast cancer, *Dalton Trans.*, 2021, **50**(42), 15389–15399.

50 A. D. Becke, Density-functional exchange-energy approximation with correct asymptotic behavior, *Phys. Rev. A*, 1988, **38**(6), 3098.

51 A. Becke, Density-functional thermochemistry. III. The role of exact exchange, *J. Chem. Phys.*, 1993, **98**, 5648.

52 T. Yanai, D. P. Tew and N. C. Handy, A new hybrid exchange–correlation functional using the Coulomb-attenuating method (CAM-B3LYP), *Chem. Phys. Lett.*, 2004, **393**(1–3), 51–57.

53 P. J. Hay and W. R. Wadt, Ab initio effective core potentials for molecular calculations. Potentials for K to Au including the outermost core orbitals, *J. Chem. Phys.*, 1985, **82**(1), 299–310.

54 P. J. Hay and W. R. Wadt, Ab initio effective core potentials for molecular calculations. Potentials for the transition metal atoms Sc to Hg, *J. Chem. Phys.*, 1985, **82**(1), 270–283.

55 A. V. Marenich, C. J. Cramer and D. G. Truhlar, Universal solvation model based on solute electron density and on a continuum model of the solvent defined by the bulk dielectric constant and atomic surface tensions, *J. Phys. Chem. B*, 2009, **113**(18), 6378–6396.

56 R. M. Khaled, D. A. Habashy, A. Y. Ahmed, O. S. Ismael, S. S. Ibrahim, M. Abdelfatah, K. Radacki and A. M. Mansour, Photoactivatable properties of water-soluble fac-Mn (CO) 3 bearing N^ O bidentate pyridine ligands, *Polyhedron*, 2022, 116048.

57 A. E. Reed, L. A. Curtiss and F. Weinhold, Intermolecular interactions from a natural bond orbital, donor-acceptor viewpoint, *Chem. Rev.*, 1988, **88**(6), 899–926.

58 M. Frisch, G. Trucks, H. Schlegel, G. Scuseria, M. Robb, J. Cheeseman, J. Montgomery, T. Vreven, K. Kudin and J. Burant, *GAUSSIAN 03. Revision A. 7*. Gaussian. Inc., Pittsburgh (PA), 2003.

59 A. Frisch, A. B. Nielson and A. J. Holder, *Gaussview User Manual*, Gaussian, Inc., Pittsburgh, PA, 2000.

60 D. Han, M. S. Denison, H. Tachibana and K. Yamada, Effects of estrogenic compounds on immunoglobulin production by mouse splenocytes, *Biol. Pharm. Bull.*, 2002, **25**(10), 1263–1267.

61 M. B. Hansen, S. E. Nielsen and K. Berg, Re-examination and further development of a precise and rapid dye method for measuring cell growth/cell kill, *J. Immunol. Methods*, 1989, **119**(2), 203–210.

62 M. Leite, M. Quinta-Costa, P. S. Leite and J. E. Guimarães, Critical evaluation of techniques to detect and measure cell death–study in a model of UV radiation of the leukaemic cell line HL60, *Anal. Cell. Pathol.*, 1999, **19**(3–4), 139–151.